PAPER

Cu/Fe embedded N-doped carbon as a highly durable oxygen reduction electrocatalyst†

Banafsha Habib,[ab] Shaowei Chen, [ID][b] Forrest Nichols,[b] Shamraiz Hussain Talib, [ID][c] Nasima Arshad, [ID][d] Anham Zafar, [ID][a] Arshad Mahmood,[e] Shahid Zaman [ID]*[f] and Naveed Kausar Janjua [ID]*[a]

Dual metal atoms embedded into carbon are emerging electrocatalysts due to synergistic interaction. Herein, copper and iron dual-atoms embedded in a nitrogen-doped carbon support with abundant metal–nitrogen moieties are fabricated *via* zinc imidazole framework pyrolysis. Hollow nitrogen-doped carbon (HNC) containing Cu/Fe–N$_x$ moieties (Cu:Fe/HNC) shows excellent oxygen reduction activity with a half-wave potential of 0.84 V in alkaline media. Furthermore, the Cu:Fe/HNC exhibits remarkable stability and strong anti-poisoning ability due to the synergistic interaction of the Cu/Fe–N$_x$ moieties in the HNC architecture. Density functional theory calculations revealed the optimum adsorption and desorption of oxygen intermediates due to the synergistic interaction of Cu–N$_x$ and Fe–N$_x$ sites, resulting in improved oxygen reduction performance. This work provides a facile synthesis of dual metal atom catalysts for developing low-cost, nonprecious metal-based ORR electrocatalysts.

Introduction

Dual atoms embedded into carbon structures are emerging electrocatalysts due to controlled morphology, and tunable catalytic and synergistic properties. Rising global energy demands and the consequent catastrophic environmental impact have triggered the search for sustainable and green energy conversion and storage technologies to minimize the reliance on fossil fuels.[1–3] Among the different renewable energy technologies, zinc–air batteries are promising due to higher power/energy density and zero emissions.[4–9] The oxygen reduction reaction (ORR) is a crucial reaction in zinc–air batteries that governs the overall performance.[10–14] However, the sluggish kinetics have limited the practical performance and durability of batteries.[15] Generally, Pt-supported carbon catalysts are used as cathode catalyst materials for the ORR despite their natural scarcity, high price and limited durability.[16] Therefore, nonprecious metal-based catalysts are an emerging alternative due to the limited stability and high cost of Pt-based catalysts.[17–21]

N-Doped carbon materials have emerged as active and durable catalyst supports due to their intrinsic activity *via* heteroatom doping and high graphitization.[22] Different nitrogen-containing precursors such as melamine, urea, and metal–organic frameworks are pyrolyzed at high temperature to form N-doped carbon as a catalytically active support template for ORR electrocatalysts.[23] Zeolitic imidazole frameworks have been widely used precursors for N-doped carbon due to unique surface geometry with a large surface area, profuse porosity and maximum nitrogen content to engineer structurally tailored NC materials.[24,25] Additionally, the N-doped carbon supports are doped with various transition metals to enhance the intrinsic catalytic properties due to M–N$_x$ synergistic moieties.[17,26–29] Such hybrid transition metal doped N-doped carbon provides a large surface area, high porosity, abundant active sites and synergistic properties.[30–32] The M-NC matrix with abundant M–N$_x$ moieties forms a unique bonding configuration between the metal atoms and N-doped carbon matrix, optimizing the adsorption of oxygen intermediates at the active sites for efficient ORR.[33–36]

Cu-Based nonprecious metal catalysts are excellent candidates for the ORR among different transition metals.[37] Theoretical studies demonstrate that Cu-based catalysts show higher ORR properties due to their close existence to Pt in a volcanic plot.[38] However, Cu-based catalysts show high diffusion coefficients resulting in dissolution, aggregation, surface oxidation, and irretrievable integration. Therefore, incorporating another

[a] Department of Chemistry Quaid-i-Azam University, Islamabad, 45320, Pakistan. E-mail: nkjanjua@qau.edu.pk
[b] Department of Chemistry and Biochemistry, University of California, 1156 High Street, Santa Cruz, California 95064, USA
[c] Department of Chemistry, Khalifa, University of Science and Technology, Abu Dhabi, P.O. Box 127788, United Arab Emirates
[d] Department of Chemistry, Allama Iqbal Open University, Islamabad, Pakistan
[e] Material Science and Engineering Division, National Institute of Laser and Optronics/PIEAS, Islamabad, 45650, Pakistan
[f] Institut d'Innovations en Écomatériaux, Écoproduits et Écoénergies, Université du Québec à Trois-Rivières, 3351 boul. des forges, Trois-Rivières, Québec G8Z 4M3, Canada. E-mail: shahid.zaman@uqtr.ca
† Electronic supplementary information (ESI) available. See DOI: https://doi.org/10.1039/d3ma00540b

nonprecious metals is envisioned to boost the ORR performance and durability of Cu-based catalysts.[39,40] Fe-doped carbon is also an excellent ORR catalyst in fuel cells and Zn air batteries, but the Fe single-atom doped carbons are vulnerable to dissolution, resulting in limited durability of the catalysts. In many of the Cu-NCs and Fe-NCs, despite having large onset potential and half-wave potential values, the biggest issue is their stability towards poisoning tests and a gradual decrease in activity.[41] A distinctive benefit of Cu/Fe-HNC is the stability and durability of this electrocatalyst in contrast to simple Cu-NC and Fe-NC. Fe incorporation into ZIF-8-derived N-doped carbon partially substitutes Zn, resulting in bimetallic M-NC for higher ORR activity and stability.[42] Thus, incorporating dual-metal atoms into NC can alleviate the poor stability of the single active sites and improve the ORR performance by synergistic interaction among the different MN_x moieties.[43]

Herein, we developed Cu/Fe dual-metals dispersed in a hollow nitrogen-doped carbon support (Cu/Fe (x:y)-HNC) through a facile pyrolysis of ZIF-8 followed by treatment with tannic acid. Different ratios of Fe:Cu were prepared and analyzed for the ORR in alkaline media and benchmarked with standard Pt/C catalysts. The morphology and electronic structure of the Cu/Fe (x:y)-HNC catalyst were characterized by advanced microscopic and spectroscopic analytical techniques. Moreover, the structure–activity relationship of Cu/Fe (x:y)-HNC has been explored by DFT studies.

Results and discussion

The crystal structure is explored by X-ray diffraction (XRD) for the different synthesized catalysts, such as HNC, Fe-HNC, and Cu-HNC, and different ratios of Cu/Fe, $i.e.$, Cu/Fe (1:1) HNC, Cu/Fe (2:1) HNC and Cu/Fe (3:1) HNC. The XRD patterns for different ratios of Cu/Fe (x:y)-HNC, Fe-HNC, and Cu-HNC and that of simple HNC show a highly amorphous structure (Fig. 1). A broad shoulder peak between $20°$ and $30°$ having a preferred orientation along the (002) planes confirmed the presence of low graphitic carbon.[44,45] Moreover, the higher degree of graphitization in the Cu:Fe doped compositions of HNC shows the formation of graphitic carbon due to Cu/Fe dual-atoms. It is worth noting that there are no noticeable Bragg peaks for metallic Cu and Fe in the XRD patterns of all the synthesized samples because of the low metal loading. Alternatively, it indicates the formation of Cu/Fe dual-atoms as $M–N_x$ moieties in the HNC, which shows the embedded Cu/Fe dual-atoms within the HNC matrix.[46]

Surface morphology and fine structural investigation are carried out via scanning electron microscopy (SEM) and Transition electron microscopy (TEM). The SEM images of the Cu/Fe(2:1)-HNC samples show the modified ZIF-8 structure in HNC as a cage-like structure with a shell-thickness and diameter around 20 nm (Fig. 2a–c). Similarly, the comparative morphology analysis of different Cu:Fe ratios shows that metal loadings substantially affect the final morphology and particle size of the Cu/Fe (x:y)-HNC catalysts (Fig. S1 and S2, ESI†). Furthermore, TEM analysis reveals the fine structure of the Cu/Fe(2:1)-HNC
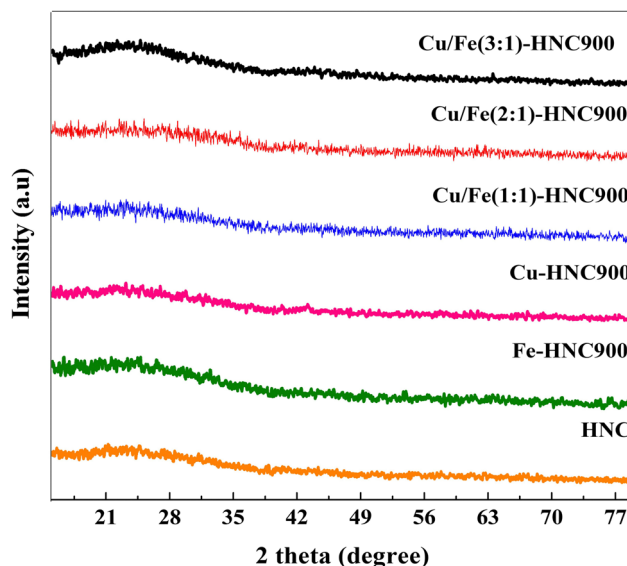

Fig. 1 XRD patterns of Fe/Cu (x:y)-HNC, Cu-HNC, Fe-HNC and HNC.

catalyst with a hollow NC architecture (Fig. 2d–f and Fig. S3, ESI†). Nanometer-sized metal particles are well dispersed in the hollow HNC matrix (Fig. 2f). Microscopy analysis reveals a uniform morphology with highly mesoporous and identical honeycomb-like hollow structures, having Cu and Fe moieties embedded on the HNC surface. These nanoparticles exhibited precise lattice-fringes with an ~0.3 nm d-spacing and Cu nanoparticles can be visualized as partially encapsulated in a carbon backbone (Fig. 2f).[11] Additionally, TEM mapping analysis further reveals dual metal (Cu and Fe) moieties embedded into a mesoporous hollow structure with a uniform distribution of all the constituents of the Cu/Fe(2:1)-HNC catalyst (Fig. 2g). Similarly, the TEM element mapping shows that all the elements C, N, Cu and Fe are homogeneously dispersed and that is the case for their stability and sustainability under the ORR.

The electronic properties of Cu/Fe(2:1)-HNC were explored by X-ray photoelectronic spectroscopy (XPS) to gain a detailed understanding of the elemental composition and valence states of the individual elements in Cu/Fe(2:1)-HNC. The broadly scanned survey spectra demonstrate the presence of Cu at 934, Fe at 710 and, N at 400 and, O at 531, and C at 285 eV, respectively, in the Cu/Fe(2:1)-HNC structural features (Fig. S4, ESI†). However, no prominent peak was identified for Zn in the survey, suggesting the evaporation of Zn at a higher temperature of 900 °C.[47,48] Furthermore, high-resolution spectra for C 1s are deconvoluted into peaks at 284.47, 285.16 and 287.84 eV corresponding to C=C (sp^2), C–C (sp^3) and C–O, C=O carbons, respectively (Fig. 3a). The sp^2 peak at ~284.47 eV as a major peak in the C 1s spectrum proposed the successful carbonization of the ZIF-8 matrix into HNC at elevated temperatures, which is facilitated by metallic species to form sp^2 carbon.[11] The relatively higher sp^2 graphitic carbon content in Cu/Fe(2:1)-HNC is ascribed to the higher pyrolysis temperature, $i.e.$, 900 °C, which is essential for catalyst durability.[49,50] Correspondingly, high-resolution spectra of N 1s are resolved into four different peaks
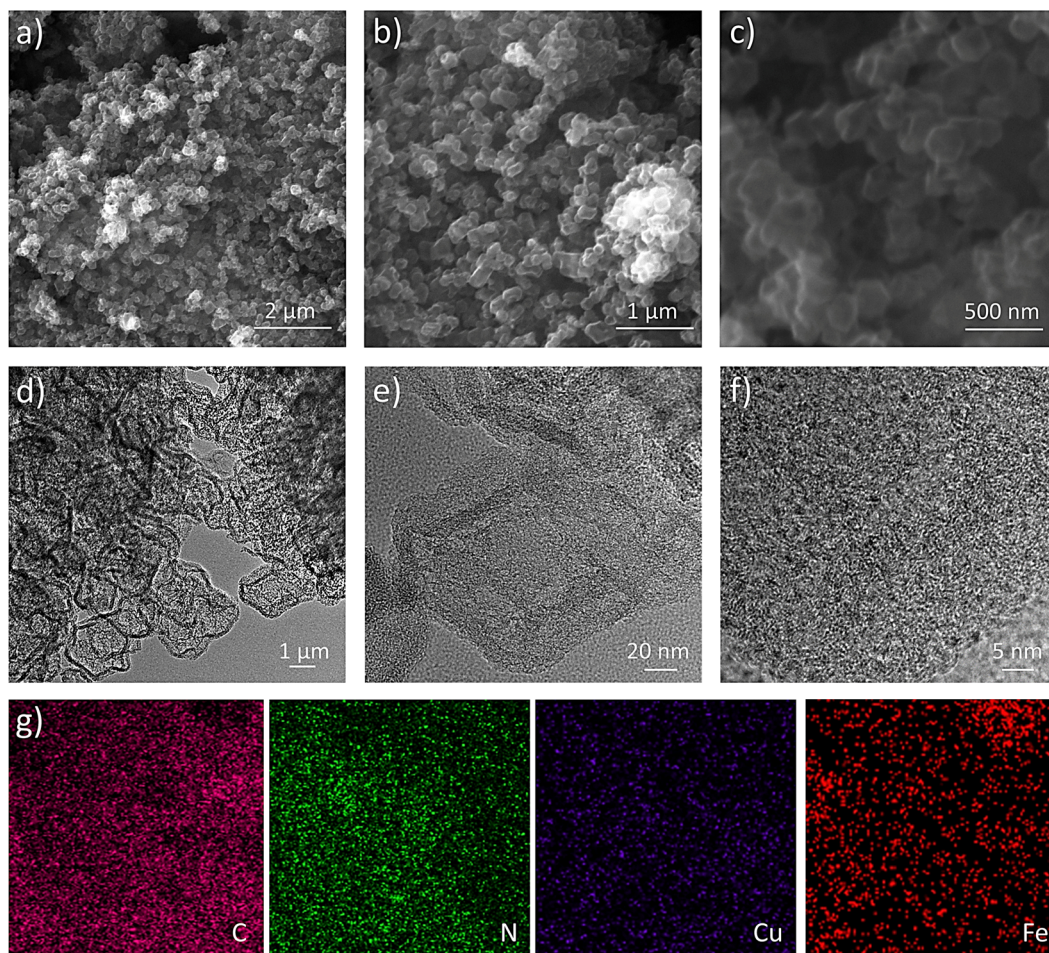
Fig. 2 Microscopic surface morphology characterizations. (a)–(c) SEM images, (d)–(f) TEM images and (g) TEM mapping of Cu/Fe(2:1)-HNC.

at 398.36, 399.60, 400.88, and 404.43 eV representing the pyridinic, M–N$_x$ (Fe–N/Cu–N), graphitic and oxidized N species, respectively (Fig. 3b).[51] Pyridinic N accounts for almost half % of overall nitrogen dopants and is proposed to be the main active site for the ORR.[52] Similarly, graphitic nitrogen is the dominant species, specifying their augmented thermal stability as well as amended geometric stabilization of the carbon structure. A prominent metal-N peak as M–N$_x$ abundantly exists as the N configuration in dual metal catalysts and acts as a potential active site for the ORR. The high-resolution Fe 2p spectrum is deconvoluted into four peaks as enunciated at 712.92, 717.64, 723.16, and 730.06 eV, which are assigned to the Fe(II) 2p$^{3/2}$, Fe(III) 2p$^{3/2}$, satellite, Fe(II) 2p$^{1/2}$, and Fe(III) 2p$^{1/2}$ peak, respectively (Fig. 3c). This observation suggested the existence of Fe in Cu/Fe(2:1)-HNC as Fe(II) and Fe(III).[53] The XPS high-resolution spectra of Cu 2p have five peaks at 932.08, 934.50, 954.17, 955.30, and 941.4 eV attributed to the Cu(I) 2p$^{3/2}$, Cu(II) 2p$^{3/2}$, satellite, Cu(I) 2p$^{1/2}$, and Cu(II) 2p$^{1/2}$ peaks, correspondingly (Fig. 3d). The Cu and Fe XPS analysis reveals the existence of Cu–Fe bonded to the N in HNC *via* different configurations in the N1s spectrum and verifies the non-existence of metallic nanoparticles in Cu/Fe(2:1)-HNC.[33] Furthermore, Fourier transform infra-red spectroscopy (FTIR) was executed to analyze the surface functionalities of the Cu/Fe

(2:1)-HNC. The FTIR spectrum implies the presence of different functional groups with corresponding structural bond formation, such as a C=C stretching vibration for sp^2 at $\sim$1450 cm^{-1} and a C–H bending vibration of Cu/Fe(2:1)-HNC (Fig. S5, ESI†).

ORR activity was evaluated on a rotating ring disk electrode in O$_2$ saturated 0.1 M KOH at the potential sweep rate of 10 mV s^{-1}. The comparative cyclic voltammetry (CV) in O$_2$ evidenced a cathodic peak in an oxygen-rich environment, while no peak is found in the N$_2$ atmosphere (Fig. S6, ESI†). Therefore, it is inferred that the reduction peak appears only due to the ability of Cu/Fe (2:1)-HNC to reduce the O–O bond at the interface of the electrode/catalyst. Similarly, the linear sweep voltammetry (LSV) curves also show that the non-zero current of the different samples begins to emerge in the reverse scan, giving evidence of adequate competency to reduce oxygen (Fig. 4a). The onset potential (E_{onset}) towards the ORR for HNC is 0.855 V with the half-wave potential ($E_{1/2}$) of 0.69 V. The benchmark standard for the ORR is Pt/C, which showed a high value for E_{onset}, 1.008 V, having a more positive $E_{1/2}$ of 0.82 V. However, there is a significant improvement in E_{onset} and $E_{1/2}$ for the other catalysts containing Cu and Fe-doped HNC, which demonstrates that the metallic species contribute substantially to the ORR activity (Fig. 4b and Table S1, ESI†). The Cu/Fe
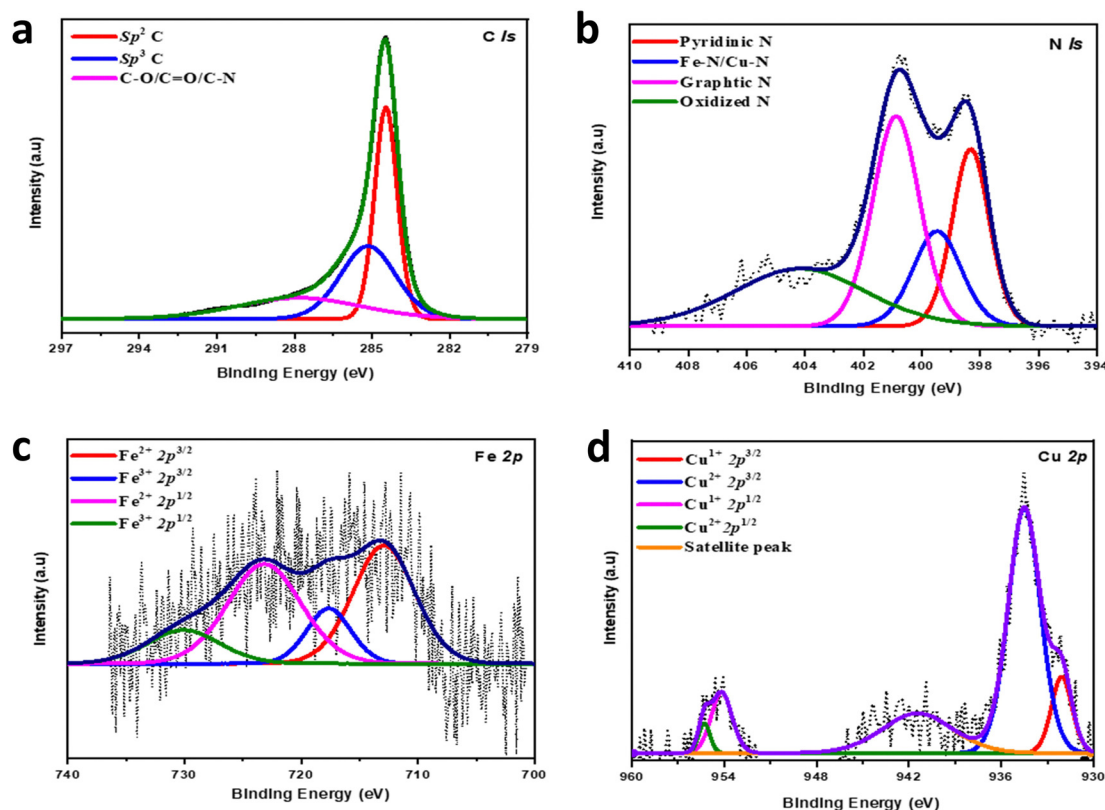
Fig. 3 Electronic structural analysis of the Cu/Fe(2:1)-HNC, and high-resolution XP spectrum of (a) C 1s, (b) N 1s, (c) Fe 2p and (d) Cu 2p.

(2:1)-HNC shows E_{onset} and $E_{1/2}$ more positive than Pt/C and all other catalysts, signifying the significant role of dual atomic sites in enhancing the ORR performance. These voltammetric parameters are promising when compared with only Co-doped material, Co-SAC/NC, where E_{onset} and $E_{1/2}$ for the ORR were observed to be 1.006 V and 0.896 V, which is among the best catalysts (Table S3, ESI†).[49] Besides the E_{onset} and $E_{1/2}$, the intrinsic activity is assessed by Tafel slope, where Cu/Fe(2:1)-HNC possesses a lower Tafel slope of 104 mV dec^{-1} than Pt/C (115 mV dec^{-1}), demonstrating the parallel intrinsic ORR activity (Fig. 4c). These Tafel slope values suggest that all the doped HNC catalysts show similar behavior to Pt/C, where the rate-determining step is expected to be the first electron-reduction of O–O.

Additionally, the RRDE evaluation and calculation of number of electrons "n" and H$_2$O$_2$% provides insight into the ORR selectivity towards two and four-electron pathways.[54] The n values for all the catalysts, Fe-HNC, Cu/Fe(1:1)-HNC, Cu/Fe(2:1)-HNC and 20% Pt/C are over 3.9, signifying a complete reduction of oxygen following the four-electron pathway to form OH$^-$ (Fig. 4d).[55] The ORR kinetics of the Cu/Fe(2:1)-HNC catalyst at the electrode/electrolyte interface is better in comparison to that of the HNC, Cu-HNC, and Cu/Fe(3:1)-HNC catalysts (Table S1, Fig. S7, ESI†). The comparison of J_k implied that the kinetic current density increased with increasing overpotential that was swept between +1.0 and +0.60 V (Table S2, ESI†). A maximum of −4.674 mA cm^{-2} at +0.8 V was recorded for the optimal composition, Cu/Fe(2:1)-HNC.

The durability of the Cu/Fe(2:1)-HNC catalyst was evaluated by accelerated stress testing (AST) and resistance against poisoning agents in the reaction mixture (Fig. 5a). The stability test was executed for 5000 AST in a potential range of 0.65 V to 1.05 V at 100 mV s^{-1}. The CV profiles of the Cu/Fe(2:1)-HNC catalyst modified-electrode before and after AST show that the ORR activity is affected insignificantly by vigorous AST cycling (inset Fig. 6a). Furthermore, LSV curves before and after 5000 AST cycles also show a minor difference in $E_{1/2}$ of the Cu/Fe(2:1)-HNC, demonstrating excellent electrochemical stability. Exceptional stability demonstrates the colossal durability and reproducibility of the catalyst implied from integrating Cu and Fe atoms into the NC matrix (Cu–N$_x$/Fe–N$_x$), alleviating the loss of metallic species during the ORR.

Similarly, anti-poisoning tests with KSCN and EDTA tracked electrochemical poisoning by the reactive intermediates as poisoning agents. The results suggested that Cu/Fe–N$_x$ moieties partook in the ORR activity; however, the main contributor was observed to be Cu–N. As illustrated in Fig. 6b, when the Cu/Fe(2:1)-HNC catalyst was treated with 10 mM EDTA in 0.1 M KOH solution in the presence of O$_2$, the change in $E_{1/2}$ and limiting current density is negligible, indicating the excellent stability of the catalyst towards EDTA poisoning. Furthermore, KSCN solution was also used to investigate the poisoning of the catalyst, which involves the adsorption of the SCN$^-$ ions onto the metal species and M–N$_x$ active sites and may block the active sites available for the reduction of O$_2$, thus
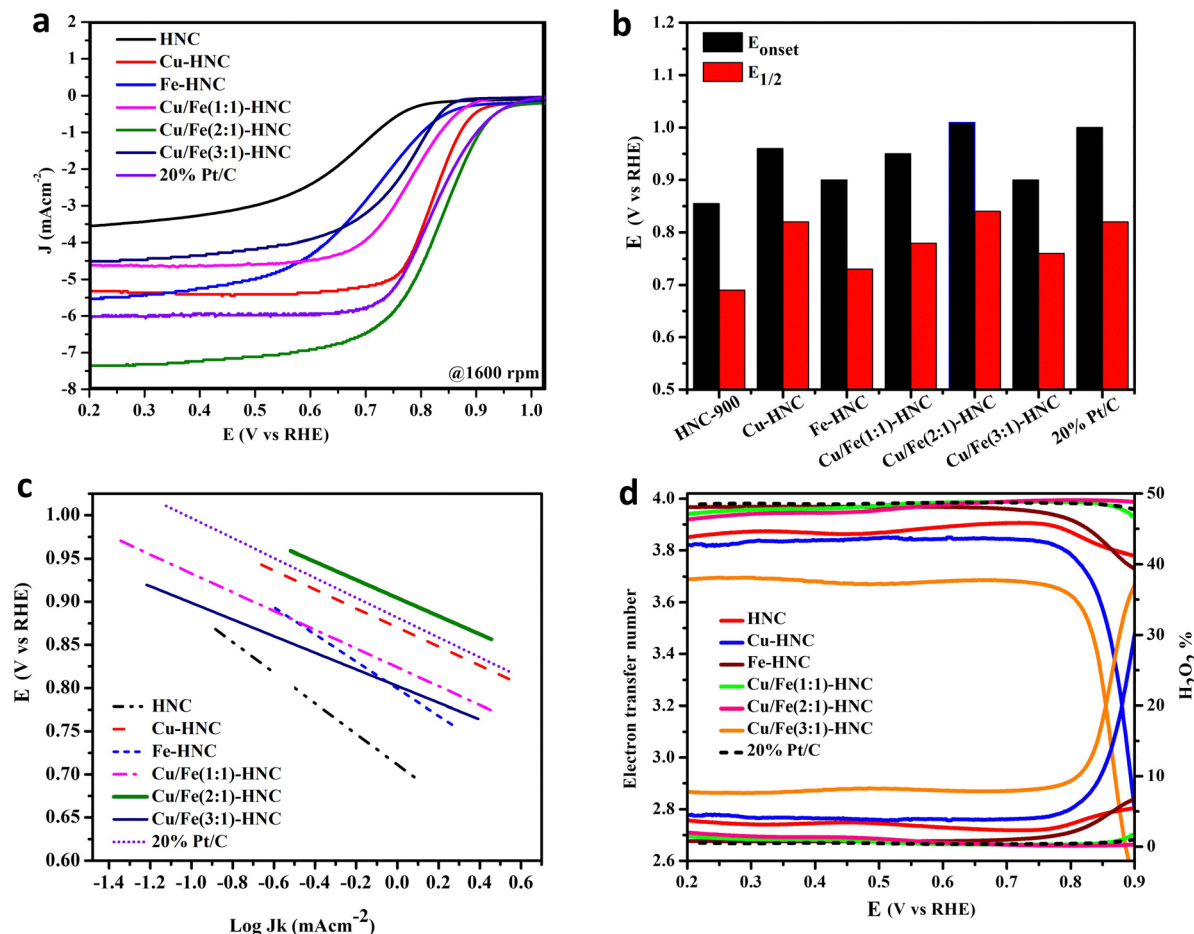
Fig. 4 ORR performance evaluation, (a) LSV curves of HNC, Cu-HNC, Fe-HNC, Cu/Fe(1:1)-HNC, Cu/Fe(2:1)-HNC and Cu/Fe(3:1)-HNC in O_2 saturated 0.1 M KOH at a rate of 1600 rpm. (b) List of E_{onset} and $E_{1/2}$ of the Cu/Fe-HNC series compared with 20% Pt/C and simple HNC. (c) Tafel slope for the different catalysts, (d) RRDE evaluation for the electron-transfer number (n) and H_2O_2 percentages of all the catalysts.
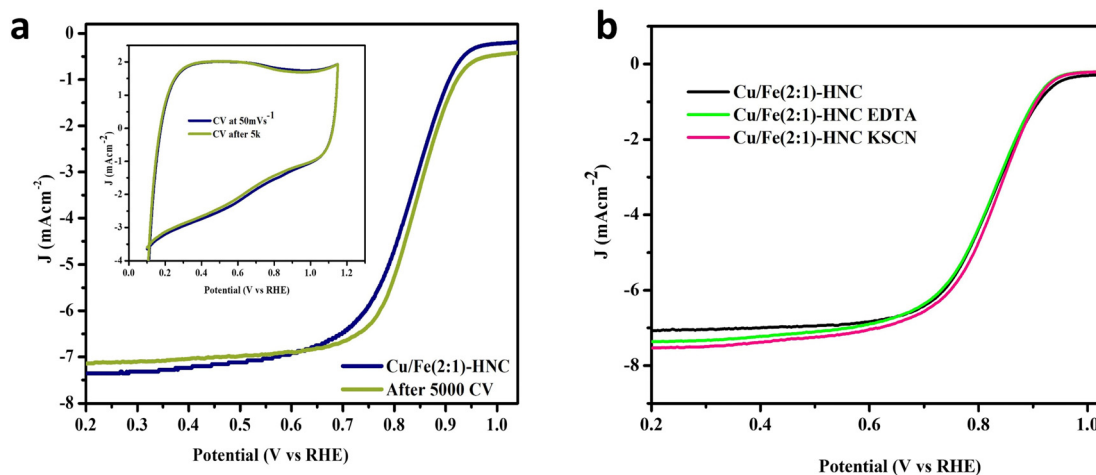

Fig. 5 Stability tests of Cu/Fe (2:1)-HNC *via* accelerated stress testing for 5000 potential cycles in N_2 saturated 0.1 M KOH. Inset (a) cyclic voltammograms and LSV curves before and after 5000 cycles at a scan rate of 50 mV s^{-1} (b) anti-poisoning test of Cu/Fe (2:1)-HNC with EDTA and KSCN treatments in 0.1 M KOH.

affecting the activity of the catalyst. Again, no change has been observed in the $E_{1/2}$ value of the Cu/Fe(2:1)-HNC catalyst after its treatment with KSCN. This infers that the Cu/Fe–N$_x$ active centers of the catalyst couldn't be poisoned by SCN$^-$ ions and provide evidence about the stability and reproducibility of the catalyst Cu/Fe(2:1)-HNC under harsh chemical environments.
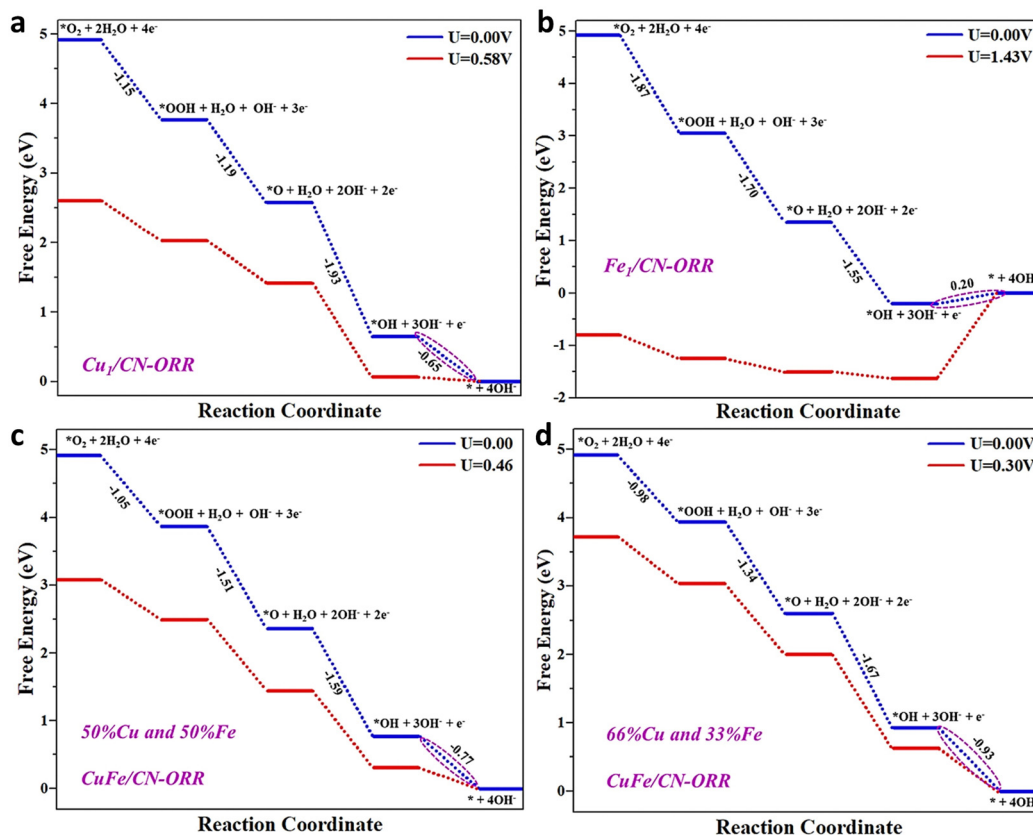
Fig. 6 The calculated potential free energy diagrams of the ORR at different potentials catalyzed by: (a) Fe/NC, (b) Cu/NC, (c) Cu_xFe_x/NC (x = 50% Fe and 50% Cu), and (d) $Cu_{2x}Fe_x$/NC (x = 33% Fe and 66% Cu) for different up and downhill behaviors during the ORR. The pink circle represents the rate-limiting step of the elementary reactions.

Thus, the stability tests imply that the interactions between the active sites (Cu–N_x and Fe–N_x moieties) and HNC are robust and corrosion-resistant. Moreover, electrochemical impedance spectroscopy (EIS) analysis was also carried out for all the glassy carbon-modified electrodes in 1 M KOH (Fig. S8, ESI†). The EIS performance of Cu/Fe(2 : 1)-HNC and Cu/Fe(3 : 1)-HNC is inferred to be at par with respect to the mass transport coefficient, mT value of ∼1.3 × 10^{-4} cm s^{-1} (Table S4, ESI†). The diffusion coefficient value of the Cu/Fe(2 : 1)-HNC composition is maximum, while the semi-circular behavior with minimum resistance can be observed for the Cu/Fe(2 : 1)-HNC as compared to other catalysts, which conforms to the improved ORR activity

Computational studies were carried out to gain further insight into the individual role of Cu and Fe atoms and synergistic interaction towards the ORR. DFT calculations on Fe/NC, Cu/NC and Cu_xFe_x/NC (x = different percentage ratios of Fe and Cu co-doped atoms) surfaces were performed to justify the utmost enhancement in the ORR activity. Here, the surface of NC was modeled using a 2 × 2 × 1 supercell comprising 24 nitrogen (N) and 24 carbon (C) atoms, generating a hole encircled by six sp^2 bonded N atoms, which are beneficial for Fe/Cu anchoring. After structural optimization, the anchored Fe and Cu bonds with two N edge atoms keep the NC planar geometric configuration undistorted. The calculated binding energies (E_b) between the anchored metal atoms [Fe (−4.48 eV),

Cu (−3.15 eV)] and NC surface are negative. The large E_b value indicates that Fe and Cu atoms actively bind on the NC surface with high stability. Furthermore, the charge density difference analysis illustrates significant electron transfers from the bonded metal atoms to the adjacent N atoms of the NC surface, primarily responsible for the robust E_b.

Generally, the entire ORR reaction contains four concerted adsorption and desorption steps over the M/NC surface site. In the first step, the adsorbed O_2* is protonated to OOH* (the asterisk signifies the adsorption site) species on the catalyst surface. In the second step, protonation occurs after the O–O bond cleavage, resulting in the departure of the H_2O molecule while the atomic oxygen (O*) remains on the catalyst surface. In the third step, the adsorbed O* is hydrogenated to the OH* species by accumulating another proton-coupled electron transfer step. Finally, the OH* species are protonated to form another H_2O molecule. Precisely, we calculated the corresponding Gibbs free energies (ΔG) of OOH, O and OH species, the main ORR intermediates dominating the inclusive ORR activity.

The potential energy profile based on the proposed reaction pathway and the adsorption configuration on the M/NC surface shows that all of the ORR steps for the M/NC surface are downhill at zero potential (U = 0 V), signifying that the reaction proceeds spontaneously. The Cu/NC catalyst, with a positive value of ΔG_{OH*} of 0.58 V, possesses superb catalytic activity for

the ORR, with the fourth step (OH* → H₂O) being the rate-determining step (Fig. 6a). As shown in Fig. 6b, the Fe/NC catalyst has a negative ΔG_{OH^*} value and a high overpotential. The high overpotential indicates a robust interaction between the Fe atom and OH* species, which will hinder the formation of H₂O in the final step.[55] For Fe/NC, the four steps were found to be the potential-limiting step (OH* → H₂O), and the calculated overpotential is 1.43 V. This catalyst is unsuitable for the ORR due to strong OH* adsorption and high overpotential. To further improve the ORR catalytic activity on the NC surface, we have used different co-doping ratios of Cu and Fe atoms on the NC surface.[56] Two different ratios of Fe and Cu were considered: (i) the equal ratio of Fe (50%) and Cu (50%) co-doped on the NC surface (Cu$_x$Fe$_x$/NC); (ii) the double ratio of Cu (66%) and the single ratio of Fe (33%) co-doped on the NC surface (Cu$_{2x}$Fe$_x$/NC) was taken. In the case of the Cu$_x$Fe$_x$/NC (x = 50% and 50%) catalyst, the fourth step (OH* → H₂O) is the rate-limiting step with the overpotential of 0.46 V. Meanwhile, for the Cu$_{2x}$Fe$_x$/NC (x = 66% and 33%) systems, the fourth step (OH* → H₂O) is also the rate-limiting step with the overpotential of 0.30 V (Fig. 6c and d). Compared with the Cu/NC catalyst, we can accomplish that an increased percentage ratio of Cu atoms weakens the interaction between the OH* and Cu$_x$Fe$_x$/NC catalyst and enhances the ORR activity. The low overpotential implies that the ORR is favored when a high Cu ratio takes the role of the catalytic active site. The above results suggest that the co-doped Cu$_{2x}$Fe$_x$/NC (x = 66% and 33%) system is a promising catalyst for the ORR, and the theoretical data agree with the experimental results.

Conclusions

Potentially viable ORR electrolysis is being reported for a series of nonprecious bimetallic Cu and Fe dual-atoms dispersed into hollow nitrogen-doped carbon catalytic platforms synthesized *via* ZIF pyrolysis. The prepared Cu/Fe(2:1)-HNC exhibited excellent ORR activity and remarkable stability with high anti-poisoning ability against KSCN and EDTA, attributed to synergistic catalysis *via* Cu and Fe bimetallic dual-atoms. Additionally, the experimental results were corroborated through DFT calculations, which evidenced that Cu/Fe(2:1)-HNC systems have higher activity with a lower overpotential value of 0.30 V of the rate-limiting step. The DFT-derived large binding energies, E_b, indicate that the dual metals, Fe and Cu, actively bind on the NC surface with high stability. Furthermore, these stronger binding and stable composite nanomaterials have been attributed to the significant electron transfers from the bonded metal atoms to the adjacent N atoms of an NC surface, which is primarily responsible for the robust E_b as illustrated by the charge density difference analysis.

Author contributions

N. K. Janjua and S. Zaman conceived the idea. B. Habib designed and performed experiments. B. Habib and N. K Janjua co-wrote the

manuscript. N. K Janjua and S. Zaman edited and revised the manuscript. F. Nichols and S. Chen helped in characterizations. S. Talib, N. Arshad, A. Zafar and A. Mahmood assisted in the revision. All authors participated in the manuscript discussion.

Conflicts of interest

The authors declare that there is no conflict of interest regarding this article.

References

1 X. Luo, X. Wei, H. Wang, W. Gu, T. Kaneko, Y. Yoshida, X. Zhao and C. Zhu, *Nano-Micro Lett.*, 2020, **12**, 1.
2 S. Ding, M. J. Hülsey, J. Perez-Ramirez and N. Yan, *Joule*, 2019, **3**, 2897.
3 H. Wei, D. Cui, J. Ma, L. Chu, X. Zhao, H. Song, H. Liu, T. Liu, N. Wang and Z. Guo, *J. Mater. Chem. A*, 2017, **5**, 1873.
4 S. Zaman, L. Huang, A. I. Douka, H. Yang, B. You and B. Y. Xia, *Angew. Chem., Int. Ed.*, 2021, **133**, 17976.
5 J. Guo, Y. Li, Y. Cheng, L. Dai and Z. Xiang, *ACS Nano*, 2017, **11**, 8379.
6 B. Zhu, P. Lund, R. Raza, J. Patakangas, Q.-A. Huang, L. Fan and M. Singh, *Nano Energy*, 2013, **2**, 1179.
7 X. Tian, X. F. Lu, B. Y. Xia and X. W. D. Lou, *Joule*, 2020, **4**, 45.
8 N. Borchers, S. Clark, B. Horstmann, K. Jayasayee, M. Juel and P. Stevens, *J. Power Sources*, 2021, **484**, 229309.
9 S. Khan, S. S. Shah, A. Ahmad, A. B. Yurtcan, K. M. Katubi and N. K. Janjua, *J. Electrochem. Soc.*, 2022, **169**, 076512.
10 S. K. Singh, K. Takeyasu and J. Nakamura, *J. Adv. Mater.*, 2019, **31**, 1804297.
11 B. Lu, T. J. Smart, D. Qin, J. E. Lu, N. Wang, L. Chen, Y. Peng, Y. Ping and S. Chen, *Chem. Mater.*, 2017, **29**, 5617.
12 S. Zaman, A. Douka, L. Noureen, X. Tian, Z. Ajmal and H. Wang, *Battery Energy*, 2023, **2**, 20220060.
13 W. Zhang, J. Zhu, D. Cheng and X. C. Zeng, *ACS Appl. Nano Mater.*, 2020, **3**, 2536.
14 K. H. Wu, D. W. Wang, D. S. Su and I. R. Gentle, *ChemSusChem*, 2015, **8**, 2772.
15 T. Wang, C. Yang, Y. Liu, M. Yang, X. Li, Y. He, H. Li, H. Chen and Z. Lin, *Nano Lett.*, 2020, **20**, 5639.
16 M. K. Debe, *Nature*, 2012, **486**, 43.
17 H.-W. Liang, W. Wei, Z.-S. Wu, X. Feng and K. Mullen, *J. Am. Chem. Soc.*, 2013, **135**, 16002.

18 L. Shang, Y. Liang, M. Li, G. I. Waterhouse, P. Tang, D. Ma, L. Z. Wu, C. H. Tung and T. Zhang, *Adv. Funct. Mater.*, 2017, **27**, 1606215.

19 H. Zhao and Z. Y. Yuan, *ChemSusChem*, 2021, **14**, 1616.

20 N. Reddy Samala and I. Grinberg, *ChemSusChem*, 2022, **15**, e202200795.

21 S. Chen, M. Cui, Z. Yin, J. Xiong, L. Mi and Y. Li, *ChemSusChem*, 2021, **14**, 73.

22 F. Kong, X. Cui, Y. Huang, H. Yao, Y. Chen, H. Tian, G. Meng, C. Chen, Z. Chang and J. Shi, *Angew. Chem., Int. Ed.*, 2022, **61**, 16290.

23 C. Zhu, H. Li, S. Fu, D. Du and Y. Lin, *Chem. Soc. Rev.*, 2016, **45**, 517.

24 Z. Geng, Y. Liu, X. Kong, P. Li, K. Li, Z. Liu, J. Du, M. Shu, R. Si and J. Zeng, *Adv. Mater.*, 2018, **30**, 1803498.

25 X. C. Huang, Y. Y. Lin, J. P. Zhang and X. M. Chen, *Angew. Chem., Int. Ed.*, 2006, **45**, 1557.

26 S. Zaman, Y. Q. Su, C. L. Dong, R. Qi, L. Huang, Y. Qin, Y. C. Huang, F. M. Li, B. You, W. Guo, Q. Li, S. Ding and B. Yu Xia, *Angew. Chem., Int. Ed.*, 2022, **61**, 202115835.

27 R. Zhou, M. Jaroniec and S. Z. Qiao, *ChemCatChem*, 2015, **7**, 3808.

28 W. An and C. H. Turner, *J. Phys. Chem. C*, 2009, **113**, 7069.

29 P. Rao, Y. Deng, W. Fan, J. Luo, P. Deng, J. Li, Y. Shen and X. Tian, *Nat. Commun.*, 2022, **13**, 5071.

30 H. Furukawa, K. E. Cordova, M. O'Keeffe and O. M. Yaghi, *Science*, 2013, **341**, 1230444.

31 S. Kitagawa, R. Kitaura and S. I. Noro, *Angew. Chem., Int. Ed.*, 2004, **43**, 2334.

32 L. Chen and Q. Xu, *Matter*, 2019, **1**, 57.

33 W. Niu, L. Li, X. Liu, N. Wang, J. Liu, W. Zhou, Z. Tang and S. Chen, *J. Am. Chem. Soc.*, 2015, **137**, 5555.

34 W. Zhang, L. Wang, L. H. Zhang, D. Chen, Y. Zhang, D. Yang, N. Yan and F. Yu, *ChemSusChem*, 2022, **15**, e202200195.

35 Q. Liu, Y. Peng, Q. Li, T. He, D. Morris, F. Nichols, R. Mercado, P. Zhang and S. Chen, *ACS Appl. Mater. Interfaces*, 2020, **12**, 17641.

36 P. Rao, D. Wu, T.-J. Wang, J. Li, P. Deng, Q. Chen, Y. Shen, Y. Chen and X. Tian, *eScience*, 2022, **2**, 399.

37 T. Asset and P. Atanassov, *Joule*, 2020, **4**, 33.

38 L. Liu, *Chem. Rev.*, 2018, **118**, 4981.

39 J. Wang, Z. Huang, W. Liu, C. Chang, H. Tang, Z. Li, W. Chen, C. Jia, T. Yao and S. Wei, *J. Am. Chem. Soc.*, 2017, **139**, 17281.

40 P. Rao, D. Wu, J. Luo, J. Li, P. Deng, Y. Shen and X. Tian, *Cell Rep. Phys. Sci.*, 2022, **3**, 100880.

41 S. Zaman, Y. Q. Su, C. L. Dong, R. Qi, L. Huang, Y. Qin, Y. C. Huang, F. M. Li, B. You and W. Guo, *Angew. Chem., Int. Ed.*, 2022, **134**, e202115835.

42 S. Li, Y. Wang, Y. Ding, Y. He, Y. Zhang, S. Li, J. Zhang and Y. Chen, *Chem. Eng. J.*, 2022, **430**, 132969.

43 A. Jafari, M. H. Alam, D. Dastan, S. Ziakhodadadian, Z. Shi, H. Garmestani, A. S. Weidenbach and Ş. Ţălu, *J. Mater. Sci.: Mater. Electron.*, 2019, **30**, 21185.

44 Y. Luo, Z. Tang, G. Cao, D. Bi, D. P. Trudgeon, A. Loh, X. Li, Q. Lai and Y. Liang, *Int. J. Hydrogen Energy*, 2021, **46**, 1997.

45 S. Zaman, *Matter*, 2023, **6**, 2632.

46 S. Gadipelli and Z. X. Guo, *ChemSusChem*, 2015, **8**, 2123.

47 Y. Li, Z. Hua, Y. Wu, Y. Zeng, Z. Qiu, X. Tian, M. Wang and E. Li, *Sens. Actuators, B*, 2018, **265**, 249.

48 X. Li, S. Duan, E. Sharman, Y. Zhao, L. Yang, Z. Zhuo, P. Cui, J. Jiang and Y. Luo, *J. Mater. Chem. A*, 2020, **8**, 10193.

49 X. Liu, S. Zou and S. Chen, *Nanoscale*, 2016, **8**, 19249.

50 S. Yang, X. Feng, X. Wang and K. Müllen, *Angew. Chem., Int. Ed.*, 2011, **50**, 5339.

51 Z. S. Wu, L. Chen, J. Liu, K. Parvez, H. Liang, J. Shu, H. Sachdev, R. Graf, X. Feng and K. Müllen, *Adv. Mater.*, 2014, **26**, 1450.

52 R. Zhou, Y. Zheng, M. Jaroniec and S.-Z. Qiao, *ACS Catal.*, 2016, **6**, 4720.

53 M. Inagaki, M. Toyoda, Y. Soneda and T. Morishita, *Carbon*, 2018, **132**, 104.

54 Y. Chen, S. Ji, S. Zhao, W. Chen, J. Dong, W.-C. Cheong, R. Shen, X. Wen, L. Zheng and A. Rykov, *Nat. Commun.*, 2018, **9**, 5422.

55 T. Yakhanthip, S. Jungsuttiwong, S. Namuangruk, N. Kungwan, V. Promarak, T. Sudyoadsuk and P. Kochpradist, *J. Comput. Chem.*, 2011, **32**, 1568.

56 H. Liu, M. Chen, F. Sun, S. Zaman, M. Wang and H. Wang, *ACS Appl. Mater. Interfaces*, 2022, **14**, 13891.